Statistical Analysis and Modeling of Material and Frequency Influence on UAV Radar Cross-Section

Tiago O. Costalonga , Vanessa P. R. Magri , Victor Fernandes

***Abstract*—This paper provides the statistical analysis and modeling of the radar cross-section (RCS) for an unmanned aerial vehicle (UAV), the DJI Phantom IV Pro, at typical radar frequencies. Using Feko® software, RCS datasets were generated for incident wave frequencies from 1 to 40 GHz and azimuth angles spanning 0° to 359°. In addition, two materials for the UAV body were considered: a perfect electric conductor (PEC) and an acrylonitrile butadiene styrene (ABS) plastic. Extreme Value, Normal, and t-Location probability distributions were assessed to model the RCS datasets and compared using log-likelihood (LLK) scores. Numerical results show that, among the candidate models considered, the Extreme Value distribution provides the highest LLK for PEC at most frequencies, whereas for the ABS model the highest-LLK distribution alternates between Extreme Value and t-Location depending on frequency. These findings highlight the impact of the electromagnetic material assumption on the RCS statistics and underscore the importance of material- and frequency-dependent statistical characterization for UAV radar applications.**

***Index Terms*—Acrylonitrile butadiene styrene (ABS) plastic, log-likelihood, perfect electric conductor (PEC), radar cross-section (RCS), unmanned aerial vehicle (UAV).**

I. Introduction

In recent years, the popularity and quantity of unmanned aerial vehicles (UAVs) have surged globally, driven largely by their growing utility in sectors such as delivery, surveillance, and photography. However, the increasing presence of UAVs near populated and sensitive areas has raised substantial safety and privacy concerns, necessitating both stringent regulations and innovative detection solutions [1], [2]. Radar detection technologies play a crucial role in identifying and tracking UAVs [3], especially in complex environments [4]. Recent studies further illustrate the versatility of radar sensing in applications ranging from environmental monitoring with X-band systems [5] to distributed UAV detection and classification using real RCS signatures [6]. Given the diversity in UAV size (ranging from millimeters to meters), shape (rounded, squared, or customized), and body composition (plastic, titanium, composites), examining the statistical behavior of a UAV's radar cross-section (RCS) is essential for understanding radar visibility across different designs and materials [7].

Within this framework, numerous studies have been dedicated to examining the RCS of UAVs. For example, [8] explored the relation between the RCS of a small fixed-wing UAV and the detection capabilities of an anti-UAV system. They conducted simulations of the UAV's monostatic RCS using actual specifications of two radars, operating at frequencies between $8.70 - 9.65$ GHz and $3 - 16$ GHz. The results indicated that the average RCS values were -17.62 dBsm and -22.77 dBsm, respectively, resulting in a maximum detection range of 1784 m. In [9], the authors evaluated and measured the monostatic RCS of nine diverse UAV models in an anechoic chamber, with frequency ranges from 26 GHz to 40 GHz. Their findings suggest that carbon fiber UAVs are more detectable than those made of plastic or styrofoam. Also, [10] studied UAV detection by an X-band radar. For this, they have simulated a quadrotor's RCS and used the mean value to determine its maximum detection range. The difference between field measurements and simulations was approximately 70 m when using the mean RCS value. Furthermore, [11] introduced a method for UAV classification using the monostatic RCS dataset of [9], employing a novel deep learning approach known as long- and short-term memory adaptive learning rate optimization (LSTM-ALRO). This method achieved a detection accuracy of 99.88%, surpassing the performance of existing UAV classification models. Moreover, [12] investigated the statistical characteristics of the RCS of nine commercial UAVs, measuring their monostatic RCS at 9 GHz in an anechoic chamber. They concluded that the RCS patterns of the UAVs studied tend to resemble a random variable more closely than a real number. In [13], the authors performed a statistical analysis of the RCS of the DJI Phantom IV Pro at the X-band frequency. The simulations were compared with a radar system operating at 9.41 GHz from the Furuno® company. Using three typical statistical criteria, they concluded that its RCS can be modeled as an Exponential probability distribution.

Although previous studies have statistically characterized UAV RCS and demonstrated its dependence on frequency, polarization, aspect angle, and target characteristics, the isolated influence of material composition on the statistical behavior of the RCS remains a research gap. In particular, comparisons involving different UAVs may combine the effects of geometry and material, making it difficult to identify how the electromagnetic material model itself modifies the resulting RCS statistics. This work addresses this aspect through a controlled comparison in which the UAV geometry, polarization,

Tiago O. Costalonga is with the Admiral Alexandrino Instruction Center, Brazilian Navy, Rio de Janeiro, RJ, 21012-350, Brazil. (e-mail: tiago.ogioni@marinha.mil.br). ORCID: 0000-0001-5967-7719.

Vanessa P. R. Magri and Victor Fernandes are with the Telecommunication and Electrical Engineering Department, Fluminense Federal University, Niterói, RJ, 24210-240, Brazil (email: vanessamagri@id.uff.br; fernandesvictor@id.uff.br). ORCID: V. P. R. Magri, 0000-0002-8151-215X and V. Fernandes 0000-0001-5179-0645.

Digital Object Identifier: 10.14209/jcis.2026.19.

Submission: 2026-02-22, First decision: 2026-08-03, Acceptance: 2026-11-19, Publication: 2026-11-25.

observation angles, and simulation procedure are maintained unchanged, while the body material is varied between an ideal PEC representation and a frequency-dependent dielectric ABS model over the 1-40 GHz frequency range. Therefore, rather than proposing a new statistical method, this work investigates how the material assumption affects not only the RCS magnitude and variability but also the statistical model selected to represent its fluctuations.

From this perspective, this work has the following contributions:

- To characterize the frequency-dependent statistical behavior of the DJI Phantom IV Pro RCS over a broad frequency range from 1 to 40 GHz and a complete 360° azimuthal domain.
- To show the influence of the electromagnetic material through a controlled comparison between PEC and frequency-dependent ABS models while maintaining the same UAV geometry, polarization, observation angles, and simulation procedure.
- To demonstrate that the material assumption affects not only the RCS magnitude and variability but also its statistical behavior and the probability model selected within the investigated candidate set, highlighting a limitation of interpreting UAV RCS statistics obtained solely from ideal PEC representations.

The remainder of this work is organized as follows: Section II introduces the mathematical formulation of the chosen criterion for evaluating the statistical modeling and selecting the best-modeling probability distribution. Section III presents the methodology of statistical analysis and modeling. Section IV discusses the numerical results and Section V provides final remarks.

II. Mathematical Formulation

Maximum likelihood estimation (MLE) is a method for estimating the parameters of a probability distribution that best fits a given dataset. This is achieved by maximizing a likelihood function so that, under the assumed probability distribution, the observed data are the most probable. In other words, the parameters of each candidate probability distribution are varied, and the distribution that yields the highest likelihood score is selected based on the histogram of dataset samples [14].

Let $\mathcal{S}_{pd} = \{pd_0, pd_1, \ldots, pd_{D-1}\}$ represent a set of D candidate probability distributions, where each distribution pd_ℓ has parameters $\boldsymbol{\alpha}_\ell = \{\alpha_{\ell,0}, \alpha_{\ell,1}, \alpha_{\ell,2}, \ldots, \alpha_{\ell,K_\ell-1}\}$, with K_ℓ being the number of parameters for the ℓ-th distribution and $\ell \in \{0, 1, \ldots, D-1\}$. Given an independent and identically distributed (i.i.d.) random sample dataset $\boldsymbol{x} = \{x_0, x_1, x_2, \ldots, x_{N_S-1}\}$, the likelihood of parameters for the ℓ-th probability distribution is given by [15]

$$\mathcal{L}(\boldsymbol{\alpha}_\ell) = \prod_{i=0}^{N_S-1} f(\boldsymbol{\alpha}_\ell | x_i), \tag{1}$$

where $f(\boldsymbol{\alpha}_\ell | x_i)$ is the likelihood of parameters $\boldsymbol{\alpha}_\ell$ for a single outcome $x_i \in \boldsymbol{x}$.

In practice, it is often convenient to work with the natural logarithm of the likelihood function, known as the log-likelihood (LLK), which is expressed as

$$\mathrm{LLK}(\boldsymbol{\alpha}_\ell) = \ln\{\mathcal{L}(\boldsymbol{\alpha}_\ell)\} = \sum_{i=0}^{N_S-1} \ln\{f(\boldsymbol{\alpha}_\ell | x_i)\}. \tag{2}$$

Since the logarithm is a monotonic function, maximizing $\mathrm{LLK}(\boldsymbol{\alpha}_\ell)$ is equivalent to maximizing $\mathcal{L}(\boldsymbol{\alpha}_\ell)$. Once $\mathrm{LLK}(\boldsymbol{\alpha}_\ell)$ is maximized, the optimal parameters for the ℓ-th probability distribution are obtained from

$$\hat{\boldsymbol{\alpha}_\ell} = \arg\max_{\boldsymbol{\alpha}_\ell} \mathrm{LLK}(\boldsymbol{\alpha}_\ell). \tag{3}$$

For simplicity, denote the maximum LLK score for the ℓ-th probability distribution as

$$\mathrm{LLK}_\ell = \mathrm{LLK}(\hat{\boldsymbol{\alpha}_\ell}). \tag{4}$$

To identify the probability distribution that best models the dataset, the value of LLK_ℓ is first maximized across all candidate distributions

$$\mathrm{LLK}_{\max} = \max_{\ell \in \{0,1,\ldots,D-1\}} \mathrm{LLK}_\ell. \tag{5}$$

Then, the index ℓ_0 is determined as

$$\ell_0 = \{\ell \,|\, \mathrm{LLK}_\ell = \mathrm{LLK}_{\max}\}, \tag{6}$$

in which the probability distribution pd_{ℓ_0}, with optimized parameters $\hat{\boldsymbol{\alpha}_{\ell_0}}$, is chosen as the best modeling distribution for representing the dataset.

III. Methodology

This section presents the main characteristics of the UAV under simulation, the DJI Phantom IV Pro, along with the steps and parameters involved in the simulation and generation of RCS datasets. Additionally, it introduces the candidate probability distributions for modeling the datasets.

A. UAV under Simulation

The UAV investigated in this work is the Phantom IV Pro, from the DJI® company, as illustrated in Fig. 1. Its dimension is approximately $25 \times 25 \times 20$ cm (width × depth × height), being its body size (L) approximately 35 cm diagonally. DJI Phantom IV Pro weighs 1.38 kg including the battery and propellers [16]. It is primarily made of acrylonitrile butadiene styrene (ABS) plastic due to its lightweight, durable, and impact-resistant properties, which enhance flight performance, maneuverability, and resilience to rough landings.

B. RCS Datasets

The RCS datasets were created using Feko® software from Altair®. The Phantom IV Pro model is the same size as the real one. In the simulations, the UAV body was first considered as a perfect electric conductor (PEC) and then as ABS plastic. For the ABS case, the material was modeled as a frequency-dependent dielectric using the experimentally



Fig. 1. DJI Phantom IV Pro.

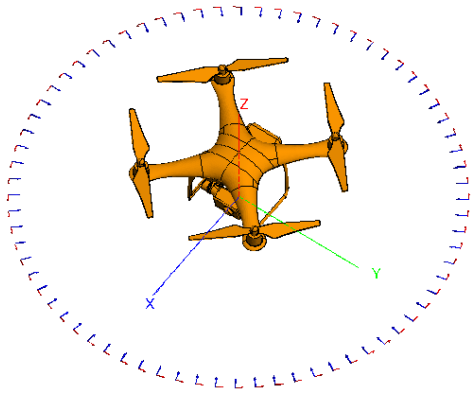


Fig. 2. Illustration of the RCS simulation of DJI Phantom IV Pro in Feko.

characterized electromagnetic properties reported in [17]. The relative permittivity was defined as $\varepsilon_r = 2.670$, 2.655, 2.638, and 2.610 at 1, 10, 25, and 67 GHz, respectively, with a dielectric loss tangent of $\tan\delta = 0.009$. Linear interpolation between these frequency points was employed in Feko. The solution method employed was ray launching - geometrical optics (RL-GO), which allows the inclusion of face-absorbing properties.

The simulation was performed using horizontal polarization, considering a monostatic RCS configuration with the incidence of plane waves in the far field region on the 3D model of the UAV at a fixed elevation angle, θ, as shown in Fig. 2. The assumed azimuth angles and frequencies of the incident wave are indicated as, respectively, $\boldsymbol{\phi} = \{\phi_0, \phi_1, \phi_2, \ldots, \phi_{N-1}\}$ and $\boldsymbol{f} = \{f_0, f_1, f_2, \ldots, f_{M-1}\}$,where N and M represent the quantity of simulated azimuth angles and incident frequencies, respectively.

The rotor orientation relative to the UAV arms was kept fixed throughout the simulations, as illustrated in Fig. 2. Nevertheless, the complete 360° azimuthal sweep continuously changes the aspect angle between the incident wave and the propeller blades, thereby sampling a broad range of blade-aspect conditions in the resulting RCS datasets. The dependence of propeller scattering on blade orientation and incident-wave polarization has also been demonstrated through electromagnetic simulations and measurements in [18]. This azimuthal variation should not, however, be interpreted as an independent variation of the rotor angular position, since rotating the blades relative to the supporting arms changes their relative geometry and may modify the combined scattering from the blades, arms, and body. Therefore, the statistical results reported here are conditional on the rotor configuration shown in Fig. 2.

The RCS data is represented by $\boldsymbol{\Sigma}^{\mathrm{b}} \in \mathbb{R}^{M\times N}$ as

$$\boldsymbol{\Sigma}^{\mathrm{b}} = \begin{bmatrix} \sigma^{\mathrm{b}}_{0,0} & \sigma^{\mathrm{b}}_{0,1} & \cdots & \sigma^{\mathrm{b}}_{0,N-1} \\ \sigma^{\mathrm{b}}_{1,0} & \sigma^{\mathrm{b}}_{1,1} & \cdots & \sigma^{\mathrm{b}}_{1,N-1} \\ \vdots & & \ddots & \vdots \\ \sigma^{\mathrm{b}}_{M-1,0} & \sigma^{\mathrm{b}}_{M-1,1} & \cdots & \sigma^{\mathrm{b}}_{M-1,N-1} \end{bmatrix}, \tag{7}$$

in which $\mathrm{b} \in \{\text{PEC, ABS}\}$ refers to the PEC or ABS plastic body material.

In (7), each element $\sigma^{\mathrm{b}}_{i,j}$ represents the RCS value for the i-th frequency and j-th azimuth angle associated with the b-th body material, being $i = 0, 1, \ldots, M-1$ and $j = 0, 1, \ldots, N-1$. The datasets of RCS values, that are statistically analyzed and modeled in this work, are given by $\boldsymbol{\sigma}^{\mathrm{b}}_i \in \boldsymbol{\Sigma}^{\mathrm{b}} \,|\, \boldsymbol{\sigma}^{\mathrm{b}}_i = \{\sigma^{\mathrm{b}}_{i,0}, \sigma^{\mathrm{b}}_{i,1}, \ldots, \sigma^{\mathrm{b}}_{i,N-1}\}$. The RCS datasets are investigated for all simulated azimuth angles at a given frequency and body material. That is, each element of $\boldsymbol{\sigma}^{\mathrm{b}}_i$ is the RCS value for a single azimuth angle ($\phi_j \in \boldsymbol{\phi}$) and a chosen frequency ($f_i \in \boldsymbol{f}$), associated with the b-th body material.

The electromagnetic model focuses on the external UAV body and does not explicitly include internal conductive components, such as the battery, motors, wiring, and electronic circuits. For the ABS case, these components could contribute additional scattering due to field penetration through the dielectric body; therefore, their omission constitutes a limitation of the present model.

C. Numerical Validation and Mesh-Sensitivity Analysis

To assess the numerical reliability of the RL-GO simulations, an analytical benchmark and mesh-sensitivity analysis was performed using a perfectly electrically conducting (PEC) sphere. Spheres are particularly suitable for computational electromagnetics validation because their symmetry and analytical solution provide a well-defined reference for identifying numerical and discretization effects [19]. The electrical size of the sphere is characterized by

$$ka = \frac{2\pi a}{\lambda} = \frac{2\pi a f}{c}, \tag{8}$$

where a is the sphere radius and k is the free-space wavenumber. The numerical monostatic RCS was compared with the analytical Mie-series solution for a PEC sphere [20], which approaches the optical-limit value

$$\sigma_{\mathrm{PEC}} \to \pi a^2 \qquad (ka \gg 1). \tag{9}$$

Mesh sensitivity was additionally assessed from the angular variability of the numerical RCS. Since the analytical RCS of a homogeneous sphere is azimuthally invariant, variations with incidence angle provide an indicator of discretization-induced numerical variability [19]. This variability was quantified by the coefficient of variation

$$CV = 100\frac{s_\sigma}{\overline{\sigma}}, \tag{10}$$

where $\overline{\sigma}$ and s_σ are, respectively, the mean and standard deviation of the angular RCS samples evaluated in linear units. The mean RCS was subsequently converted to dBsm for comparison with the analytical solution.

D. Candidate Probability Distributions

A broader screening of probability distributions for the statistical modeling of UAV RCS was previously performed by the authors in [21], considering Exponential, Gamma, Generalized Extreme Value, Generalized Pareto, Log-normal, Nakagami, Rayleigh, Rician, and Weibull distributions and comparing their fits using LLK, AIC, and BIC criteria. Rather than repeating this broad screening, the present work adopts a reduced set of candidate distributions with contrasting statistical characteristics to specifically investigate how frequency and body material affect the RCS statistics of the same UAV geometry.

Accordingly, the Normal distribution is considered as a symmetric light-tailed model, whereas the t-Location distribution provides a symmetric model with heavier tails. The Extreme Value distribution provides an asymmetric alternative suitable for representing pronounced tail behavior and extreme observations [22]. Together, these distributions provide distinct models in terms of symmetry and tail behavior, allowing the influence of frequency and material on the statistical characteristics of the RCS datasets to be investigated without repeating the broader distribution-screening study previously performed.

Thus, to model the datasets, consider the set of candidate probability distributions given by

$$\mathcal{S}_{pd} = \{\textit{Extreme Value}, \textit{Normal}, \textit{t-Location}\}.$$

IV. Numerical Results

The main electromagnetic simulation parameters employed to generate the DJI Phantom IV Pro RCS datasets are summarized in Tab. I.

TABLE I
ELECTROMAGNETIC SIMULATION SETUP USED FOR THE DJI PHANTOM IV PRO RCS DATASETS.

Parameter	Simulation setup
EM software	Feko®
Solution method	RL-GO
RCS configuration	Monostatic
Incident field	Far-field plane wave
Frequency range	1–40 GHz
Frequency step	1 GHz
Azimuth range, ϕ	0°–359°
Azimuth step	1°
Elevation angle, θ	0°
Polarization	Horizontal
Body material	PEC / frequency-dependent ABS
UAV mesh configuration	Standard
Rotor configuration	Fixed

This section is split into three parts. The first presents the numerical validation and mesh-sensitivity analysis of the electromagnetic simulations, the second is related to the statistical analysis, and the third addresses the statistical modeling of the RCS datasets.

A. Numerical Validation

The DJI Phantom IV Pro model employed in the RCS simulations was discretized using Feko's native *Standard* mesh configuration, resulting in 258,080 curvilinear triangular elements with average, minimum, and maximum edge lengths of approximately 0.896 mm, 6.52 μm, and 13.65 mm, respectively. To assess the numerical reliability of the adopted RL-GO approach and its sensitivity to geometrical discretization, the PEC-sphere benchmark described in Section III was performed at $f = \{1, 2, 5, 10, 20, 30, 40\}$ GHz. At each frequency, the monostatic RCS was evaluated at eight equally spaced azimuth angles, $\phi = \{0°, 45°, 90°, 135°, 180°, 225°, 270°, 315°\}$.

For the sphere benchmark, the *Coarse*, *Standard*, and *Fine* mesh configurations contained 44, 58, and 592 curvilinear triangular elements, with average edge lengths of approximately 80.60, 71.03, and 22.41 mm, respectively. For the $a = 0.1$ m sphere, the investigated frequencies correspond to electrical sizes ranging from $ka \approx 2.10$ at 1 GHz to $ka \approx 83.83$ at 40 GHz.

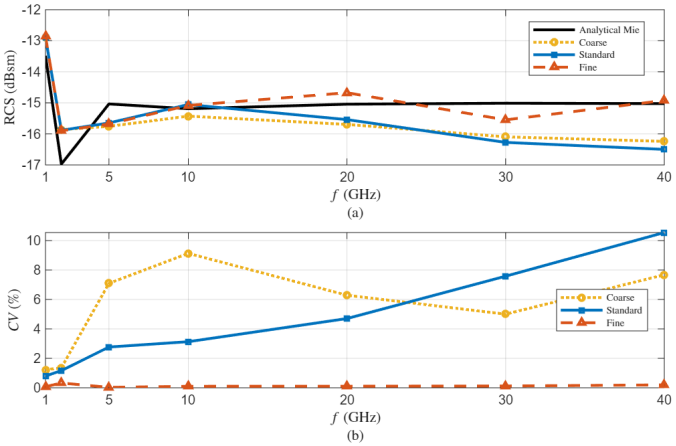


Fig. 3. Numerical validation and mesh-sensitivity analysis for a PEC sphere with radius $a = 0.1$ m. (a) Analytical Mie-series solution and mean monostatic RCS obtained with RL-GO using the Coarse, Standard, and Fine mesh configurations. (b) Coefficient of variation of the monostatic RCS over eight azimuth incidence angles for each mesh configuration.

Fig. 3(a) compares the analytical Mie-series RCS with the mean RL-GO results obtained for the three mesh configurations. At 10 GHz ($ka \approx 20.96$), the absolute differences from the analytical solution are approximately 0.14 and 0.11 dB for the *Standard* and *Fine* meshes, respectively. At smaller electrical sizes, however, comparable deviations remain for all three mesh configurations. At 2 GHz ($ka \approx 4.19$), the differences are approximately 1.11, 1.09, and 1.07 dB for the *Coarse*, *Standard*, and *Fine* meshes, respectively. The limited improvement produced by mesh refinement in this region indicates that the remaining discrepancy is predominantly associated with the high-frequency asymptotic nature of RL-GO rather than with geometrical discretization alone.

The mesh sensitivity is further evidenced in Fig. 3(b) by the angular variability of the numerical RCS. The *Fine* mesh reduced the coefficient of variation to below 0.33% throughout the investigated frequency range. Since the analytical RCS of a homogeneous sphere is azimuthally invariant, this reduction

indicates that mesh refinement substantially decreases the numerical variability introduced by the discretized representation of the curved surface, consistently with the sphere-based validation approach discussed in [19]. Overall, the benchmark supports the numerical applicability of RL-GO for electrically large targets. Conversely, the UAV RCS results at the lower-frequency end of the investigated range, where the target lies in the resonant/Mie scattering region, should be interpreted with greater caution because the high-frequency asymptotic formulation does not fully account for wave phenomena that may become relevant at small electrical sizes. These frequencies were nevertheless retained to preserve the broadband statistical analysis over the complete 1–40 GHz interval.

B. Statistical Analysis

This subsection presents the statistical analysis of RCS values generated from simulations assuming the UAV body material as PEC or ABS plastic. In this regard, Fig. 4 displays the RCS values for (a) $f_i = 9$ GHz, (b) $f_i = 18$ GHz, (c) $f_i = 22$ GHz, and (d) $f_i = 39$ GHz across all elements of $\boldsymbol{\phi}$. The blue lines represent the RCS assuming the UAV body material as PEC, while the red lines correspond to the RCS when considering the ABS plastic. Note that as the frequency increases, the variation of $\sigma_{i,j}^{\text{PEC}}$ and $\sigma_{i,j}^{\text{ABS}}$ increases. This occurs due to the decrease in the wavelength of the incident wave, resulting in numerous small parts of the UAV becoming scattering regions. Furthermore, for Fig. 4(a) and 4(b), there is a significant decrease in $\sigma_{i,j}^{\text{ABS}}$ compared to $\sigma_{i,j}^{\text{PEC}}$, with the difference being approximately 20.4 dBsm for $f_i = 9$ GHz at $\phi_j = 92°$ and 18.5 dBsm for $f_i = 18$ GHz at $\phi_j = 87°$, respectively. In contrast, for Fig. 4(c) and 4(d), the differences are close to 5.5 dBsm for $f_i = 22$ GHz at $\phi_j = 181°$ and 5.8 dBsm for $f_i = 39$ GHz at $\phi_j = 83°$, but still $\sigma_{i,j}^{\text{ABS}} < \sigma_{i,j}^{\text{PEC}}$.

To observe the behavior of the RCS when varying frequency, consider the mean and the standard deviation of RCS datasets given by

$$\overline{\sigma_i^{\text{b}}} = \frac{1}{N}\sum_{j=0}^{N-1} \sigma_{i,j}^{\text{b}} \tag{11}$$

and

$$\sigma_i^{sd,\text{b}} = \sqrt{\frac{1}{N}\sum_{j=0}^{N-1}\left(\sigma_{i,j}^{\text{b}} - \overline{\sigma_i^{\text{b}}}\right)^2}, \tag{12}$$

respectively. Fig. 5 shows the variation of $\overline{\sigma_i^{\text{b}}}$ and $\sigma_i^{sd,\text{b}}$ of the UAV's RCS datasets at different frequencies, for both PEC and ABS plastic body materials. The blue line represents the mean RCS assuming PEC, while the red line represents the mean RCS for the ABS plastic. In addition, the shaded regions around each line indicate $\overline{\sigma_i^{\text{b}}} \pm \frac{1}{2}\sigma_i^{sd,\text{b}}$, which measures the variability or uncertainty produced by the backscatter parts of the UAV.

In general, $\overline{\sigma_i^{\text{PEC}}} > \overline{\sigma_i^{\text{ABS}}}$, $\forall f_i \in \boldsymbol{f}$, which is expected since PEC is an idealized material that fully reflects incident waves. On the other hand, the ABS plastic is a dielectric material with lower conductivity, partially reflecting incident waves, resulting in lower RCS values. This difference is evident in

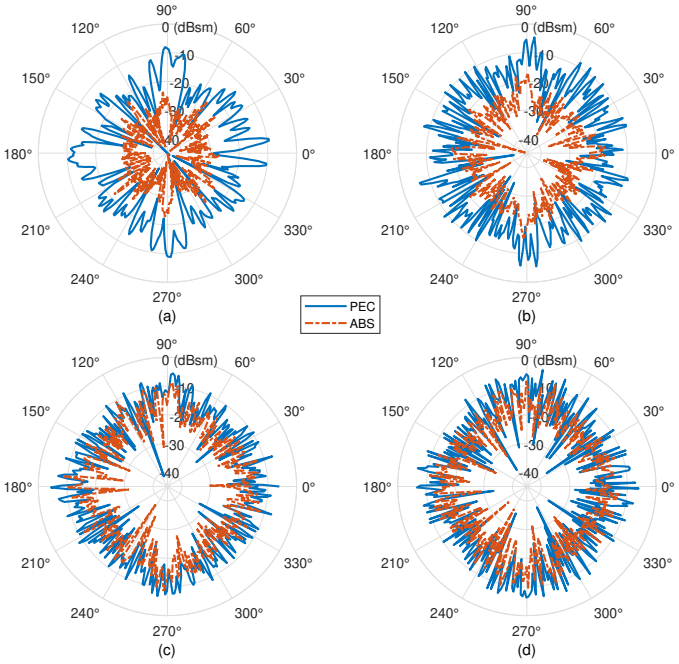


Fig. 4. RCS values for (a) $f_i = 9$ GHz, (b) $f_i = 18$ GHz, (c) $f_i = 22$ GHz, and (d) $f_i = 39$ GHz across all elements of $\boldsymbol{\phi}$.

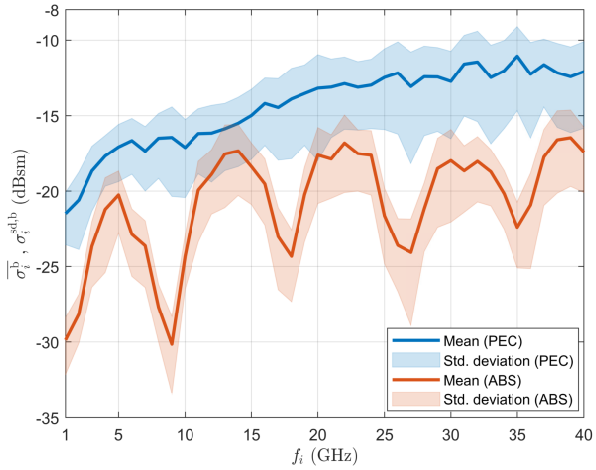


Fig. 5. Mean ($\overline{\sigma_i^{\text{b}}}$) and standard deviation ($\sigma_i^{sd,\text{b}}$) of the RCS values in terms of f_i.

the mean curves, where the ABS plastic consistently lies below the PEC across all frequencies, underscoring how the electromagnetic material assumption affects the UAV's RCS characteristics.

Notably, $\overline{\sigma_i^{\text{PEC}}}$ presents a relatively smooth curve with moderate oscillations, where $\sigma_i^{\text{sd,PEC}} > \sigma_i^{\text{sd,ABS}}, \forall f_i \in \boldsymbol{f}$. This may indicate that the PEC material's total reflection properties enhance sensitivity to frequency or orientation changes, causing more pronounced interference effects and leading to larger RCS fluctuations. The mean for the PEC material varies from approximately $\overline{\sigma_i^{\text{PEC}}} \approx -21.5$ dBsm at $f_i = 1$ GHz to $\overline{\sigma_i^{\text{PEC}}} \approx -12.4$ dBsm at $f_i = 39$ GHz, while -22.7 dBsm $< \sigma_i^{\text{sd,PEC}} < -10.5$ dBsm, $\forall f_i \in \boldsymbol{f}$.

In contrast, $\overline{\sigma_i^{\text{ABS}}}$ exhibits more pronounced oscillations, with larger fluctuations between peaks and valleys, suggesting complex interactions between incident waves and the UAV material. The peaks in $\overline{\sigma_i^{\text{ABS}}}$ range from -20.2 dBsm at $f_i = 5$ GHz to -16.4 dBsm at $f_i = 39$ GHz, and valleys from -30.1 dBsm at $f_i = 9$ GHz to -22.4 dBsm at $f_i = 35$ GHz. The ABS material's dielectric nature may absorb some incident waves, dampening reflection effects and resulting in lower standard deviation values compared to PEC, being -30.8 dBsm $< \sigma_i^{\text{sd,ABS}} < -16.2$ dBsm, $\forall f_i \in \boldsymbol{f}$. Specifically, valleys have lower standard deviations than peaks.

The frequency-dependent oscillations observed in $\overline{\sigma_i^{\text{ABS}}}$ are consistent with variations in the electromagnetic scattering response of the UAV geometry and may be associated with resonance and interference among contributions from different scattering features. The observed peaks at 5 GHz, 14 GHz, 22 GHz, 30 GHz, 32 GHz, and 39 GHz, and valleys at 1 GHz, 9 GHz, 18 GHz, 27 GHz, and 35 GHz may therefore result from frequency-dependent constructive and destructive combinations of the fields scattered by features such as the arms, body, and motor-mount regions.

Another important analysis is the kernel density estimate (KDE) of RCS datasets, comparing the PEC and ABS plastic as the UAV body material. The KDE provides a smooth and continuous curve that represents the probability density of the dataset's values, offering a clearer visualization of the distribution shape compared to the traditional histogram. This allows for a more intuitive comparison of the density of values between the different materials.

In this regard, Fig. 6 presents KDE plots for $\boldsymbol{\sigma}_i^{\text{b}}$ at different frequencies. Specifically, Fig. 6(a) and Fig. 6(b) display the KDEs for $\boldsymbol{\sigma}_i^{\text{PEC}}$ and $\boldsymbol{\sigma}_i^{\text{ABS}}$, respectively, at the frequencies $f_i = 9$ GHz, $f_i = 18$ GHz, $f_i = 22$ GHz, and $f_i = 39$ GHz.

In Fig. 6(a), the KDE curves represent the probability density of RCS datasets at specific frequencies and across all azimuth angles. At $f_i = 9$ GHz, the KDE shows a peak near -18 dBsm, with the distribution spanning from approximately -35 dBsm to -5 dBsm. As the frequency increases, the peak of the distribution shifts to higher RCS values. For instance, at $f_i = 18$ GHz, the peak is at -15 dBsm, at $f_i = 22$ GHz it is near -13 dBsm, and at $f_i = 39$ GHz, it reaches -15 dBsm. This trend indicates that higher frequencies result in higher RCS values for the PEC material.

Fig. 6(b) exhibits the KDEs for the ABS plastic UAV material at the same frequencies. The resulting distributions are noticeably different. The RCS values for ABS are shifted to lower values compared to the PEC case. At $f_i = 9$ GHz, the KDE peaks at -30 dBsm, which is much lower than for PEC. For $f_i = 18$ GHz, the distribution centers around -25 dBsm, and at $f_i = 22$ GHz, the peak is near -17 dBsm. The highest frequency, $f_i = 39$ GHz, shows a peak near -18 dBsm. Compared to PEC, the ABS plastic distributions are shifted toward lower RCS values, with their spread and shape exhibiting a stronger frequency dependence.

For further analysis, consider the aggregation of RCS values across all frequencies and azimuth angles as

$$\boldsymbol{r}_{\text{vec}}^{\text{b}} = \text{vec}(\boldsymbol{\Sigma}^{\text{b}}), \tag{13}$$

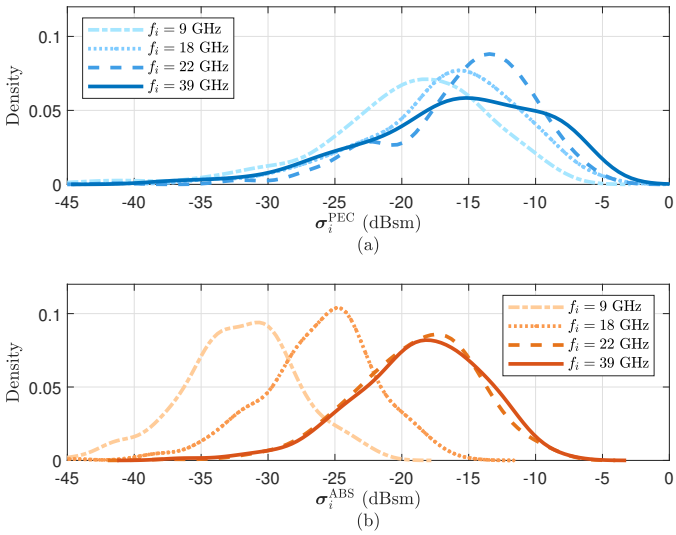


Fig. 6. KDE plots for $\boldsymbol{\sigma}_i^{\text{b}}$ at different frequencies, considering the UAV body materials as PEC and ABS plastic. (a) KDE of $\boldsymbol{\sigma}_i^{\text{PEC}}$ for $f_i = 9$ GHz, $f_i = 18$ GHz, $f_i = 22$ GHz, and $f_i = 39$ GHz; (b) KDE of $\boldsymbol{\sigma}_i^{\text{ABS}}$ for the same frequencies.

in which $\boldsymbol{r}_{\text{vec}}^{\text{b}}$ is the vector that contains all elements of $\boldsymbol{\Sigma}^{\text{b}}$, and $\text{vec}(\cdot)$ denotes the vectorization operation that reshapes a matrix into a single-column vector by stacking all columns of the matrix sequentially. This aggregation consolidates the RCS data into a single-column vector representing different frequencies and azimuth angles in one dimension.

Fig. 7 provides the KDE plots for $\boldsymbol{r}_{\text{vec}}^{\text{b}}$, given in (13), considering the UAV body materials as either PEC or ABS plastic. In this figure and assuming PEC material, the KDE curve peaks at -14.7 dBsm, with a distribution concentrated mostly from -30 dBsm to approximately -5.4 dBsm. For the ABS plastic material, despite the KDE curve peaks at a lower RCS value of -20.4 dBsm, the distribution has almost the same spread as for PEC, concentrated mostly from -35.7 dBsm to approximately -11.5 dBsm. For PEC and ABS plastic, these distributions become closer when combining RCS data across all frequencies, possibly due to an averaging effect.

Overall, the KDE for PEC tends to exhibit a broader distribution and higher variability with increasing frequency, across different angles and incidence conditions. In contrast, the KDE for ABS generally presents a narrower distribution with smaller RCS values. However, these variations tend to balance out when all frequencies are considered.

These differences in the RCS distributions also have a direct engineering interpretation in terms of UAV detectability. For fixed radar parameters and target range, the received power and, under fixed noise conditions, the SNR are proportional to σ. Therefore, greater probability mass at higher RCS values corresponds to a greater occurrence of stronger target returns, whereas increased probability in the lower-RCS region increases the occurrence of weak returns. From the basic monostatic radar equation, the minimum RCS required to exceed a receiver threshold $S_{\min}$ at range R is

$$\sigma_{\min}(R) = \frac{S_{\min}(4\pi)^3 R^4}{P_t G^2 \lambda^2}, \tag{14}$$

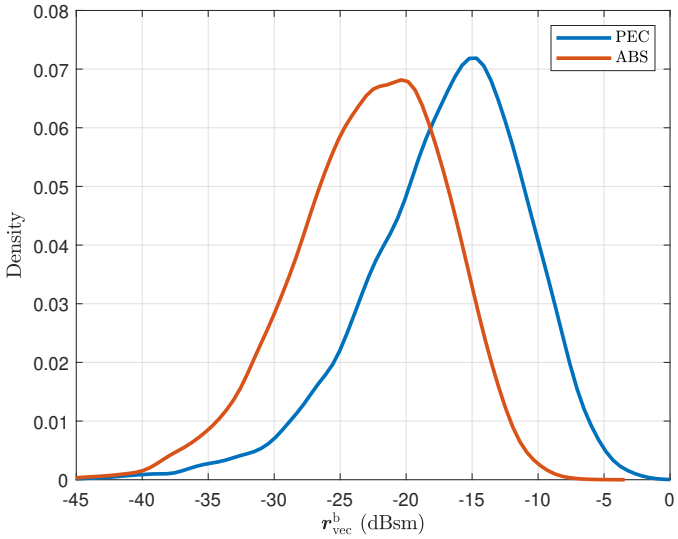


Fig. 7. KDE plots of $\boldsymbol{r}^{\mathrm{b}}_{\mathrm{vec}}$ for both PEC and ABS plastic.

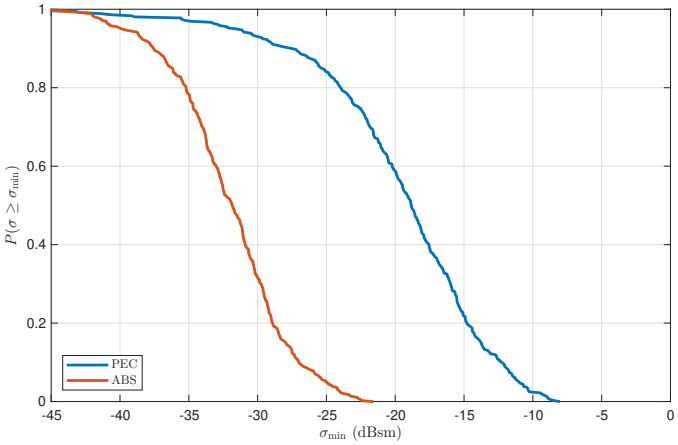


Fig. 8. Empirical RCS exceedance probability at 9 GHz for the PEC and ABS UAV models. For a specified minimum RCS $\sigma_{\min}$, the curves provide $P(\sigma \geq \sigma_{\min})$ over the simulated azimuth angles.

where $\sigma_{\min}(R)$ is the minimum RCS required at range R, in m^2; $S_{\min}$ is the minimum received power (receiver threshold), in W; R is the target range, in m; P_t is the transmitted power, in W; G is the antenna gain in linear scale (dimensionless); and λ is the wavelength, in m.

Accordingly, for an RCS distribution with CDF $F_\sigma(\sigma)$, the probability that the target RCS exceeds this threshold is $P(\sigma \geq \sigma_{\min}) = 1 - F_\sigma(\sigma_{\min})$. For comparison with the simulated RCS datasets, the threshold can be expressed in dBsm as $\sigma_{\min,\mathrm{dBsm}} = 10\log_{10}\left[\sigma_{\min}/(1\,\mathrm{m}^2)\right]$. Fig. 8 illustrates this relationship at 9 GHz, a representative frequency in the X band, using the empirical RCS samples obtained for the PEC and ABS models. The curves provide, for any specified $\sigma_{\min}$, the empirical probability over the simulated azimuth angles that the target RCS exceeds the value required to produce a received power above the corresponding receiver threshold.

As representative examples from Fig. 8, for $\sigma_{\min} = -30$ dBsm, the RCS exceeds the specified threshold for approximately 93.06% and 31.94% of the simulated azimuth angles for the PEC and ABS models, respectively. For the more restrictive threshold of $\sigma_{\min} = -25$ dBsm, these fractions decrease to approximately 84.17% and 5.00%, respectively. Therefore, the difference between the two electromagnetic material assumptions becomes particularly evident as the required minimum RCS increases.

Thus, a distribution shifted toward higher RCS values results in a higher probability of exceeding a given RCS threshold. Equivalently, since $R_{\max} \propto \sigma^{1/4}$, higher RCS values also correspond to increased potential detection ranges. This exceedance probability is not the formal radar probability of detection P_d, which additionally depends on the detector, noise/clutter statistics, integration strategy, and P_{fa}.

C. Statistical Modeling

In this subsection, statistical modeling is applied to analyze the RCS datasets of the UAV using distinct materials across multiple frequencies. By fitting several probability distributions to the RCS datasets' histogram, this modeling identifies which distribution best represents the scattering behavior of each material under different frequency conditions.

In this context, Fig. 9 shows histograms of RCS datasets for the UAV with body material as a PEC or ABS plastic, at $f_i = 9$ GHz and $f_i = 22$ GHz. Specifically, Fig. 9(a) and Fig. 9(b) represent results at 9 GHz for PEC and ABS plastic, respectively, while Fig. 9(c) and Fig. 9(d) represent results at 22 GHz also for PEC and ABS plastic, respectively. Additionally, each histogram is overlaid with Extreme Value, Normal, and t-Location probability density functions (PDFs).

In Fig. 9(a), considering PEC, at $f_i = 9$ GHz, the RCS values range primarily between -45 dBsm and -5 dBsm, peaking at -20 dBsm. The Normal and t-Location distributions align closely with the histogram peak, while the Extreme Value distribution captures the left tail better but deviates at the peak. Comparatively, in Fig. 9(b), assuming the ABS plastic, at the same frequency, the distribution is lower, with values mainly between -45 dBsm and -20 dBsm. The peak is at -30 dBsm, indicating lower RCS values due to the material change. Here, the t-Location PDF aligns closely with the RCS values, suggesting that it may provide a better fit for ABS plastic at $f_i = 9$ GHz.

For $f_i = 22$ GHz, Fig. 9(c) and Fig. 9(d) follow a similar pattern but change slightly due to frequency effects. In Fig. 9(c), assuming PEC, the RCS histogram peaks near -15 dBsm, with values distributed from -35 dBsm to -5 dBsm. The Extreme Value fits align well at this frequency, with the Normal and t-Location distributions showing a weaker fit around the peak. In contrast, Fig. 9(d), assuming ABS plastic, centers at -22.5 dBsm, indicating an increase compared to the ABS RCS values at $f_i = 9$ GHz. Again, the t-Location distribution captures the histogram shape well, particularly in the peak region, whereas the Extreme Value PDF remains better aligned with the tail.

The key takeaway from these histograms is that the t-Location distribution often provides the highest LLK among the candidate models, especially for ABS plastic, effectively capturing both the peak and tail behaviors. In contrast, the

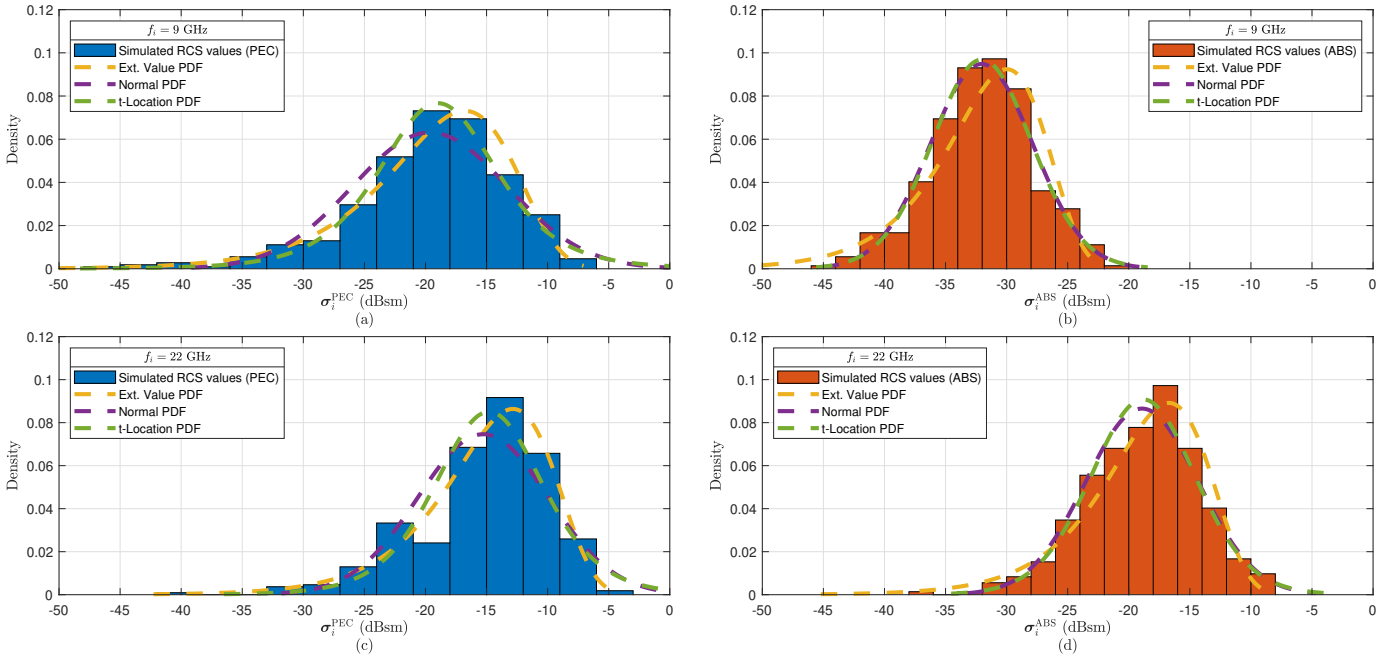


Fig. 9. Histograms of RCS values and PDFs of Extreme Value, Normal, and t-Location distributions assuming PEC and ABS as UAV body materials. (a) and (c) are for $f_i = 9$ GHz and $f_i = 22$ GHz, respectively, with the UAV body material as PEC. (b) and (d) are for $f_i = 9$ GHz and $f_i = 22$ GHz, respectively, with the UAV body material as ABS plastic.

Extreme Value distribution sometimes captures the lower tail accurately but generally fails to fit the peak area as effectively as the Normal and t-Location distributions. This fitting procedure is then extended to the complete frequency range from 1 to 40 GHz, with the highest-LLK candidate distribution identified separately at each frequency.

Then, considering the set of probability functions $\mathcal{S}_{pd}$ defined in Section III, Tab. II shows the LLK scores for each candidate probability distribution. The investigated frequencies are classified according to the IEEE Std 521-2019 radar-frequency band nomenclature [23]. Frequencies at common band boundaries are assigned to the higher-frequency band. Accordingly, the term "best-fitting distribution" used hereafter refers to the distribution achieving the highest LLK among the candidate models considered in this study, rather than to an exhaustive comparison with all possible RCS probability models. Moreover, small differences in LLK between candidate models should not be interpreted as evidence of statistically significant superiority. LLK is employed here as a relative model-selection criterion within the defined candidate set. A broader model-selection analysis using LLK, AIC, and BIC was previously conducted in [21]. The cells with the higher LLK score for each frequency are highlighted in blue for PEC and red for ABS plastic.

A band-wise inspection of Tab. II further reveals a general frequency-dependent trend in the ABS fitting results. The fraction of frequencies for which the Extreme Value distribution provides the highest LLK decreases from the lower-frequency bands toward the higher-frequency bands, while t-Location becomes predominant in Ku, K, and Ka, accounting for 66.7%, 66.7%, and 78.6% of the investigated frequencies, respectively. In contrast, no comparable band-dependent change is observed

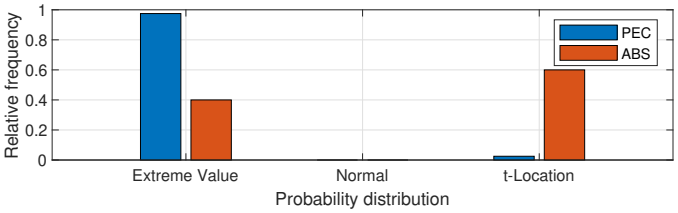


Fig. 10. Relative frequency of the best-fitting distribution for PEC and ABS plastic materials.

for PEC, for which Extreme Value provides the highest LLK at all investigated frequencies except 2 GHz. This band-wise trend further indicates that the statistical shape of the angular RCS exhibits a stronger frequency dependence for the ABS model than for the PEC model.

Fig. 10 summarizes the results of Tab. II with the relative frequency of the probability distribution that achieved the highest LLK score associated with the b-th body material

$$R^{\text{b}} = \frac{N^{\text{b}}_{\text{LLK}}}{M}, \tag{15}$$

in which, $N^{\text{b}}_{\text{LLK}}$ represents the number of times each probability distribution achieved the highest LLK score across each frequency, $f_i \in \boldsymbol{f}$.

The statistical modeling of RCS datasets assuming the body material as PEC or ABS plastic shows that the Extreme Value distribution provides the highest LLK among the candidate models considered in this study at almost all frequencies for PEC, with $R^{\text{PEC}} = 0.975$. In contrast, for ABS plastic, the distribution providing the highest LLK alternates with frequency between Extreme Value, with $R^{\text{ABS}} = 0.4$, and t-

TABLE II
LLK SCORES FOR EXTREME VALUE, NORMAL, AND T-LOCATION PROBABILITY FUNCTIONS FOR PEC AND ABS MODELS.

Band	f_i (GHz)	PEC			ABS		
		Extreme Value	Normal	t-Location	Extreme Value	Normal	t-Location
L	1	-987.00	-1022.00	-993.42	-1068.96	-1110.80	-1105.37
S	2	-1067.00	-1050.20	-1049.60	-973.28	-997.89	-997.22
	3	-1091.00	-1124.20	-1118.30	-1054.85	-1059.80	-1059.80
C	4	-1014.00	-1059.10	-1050.20	-1085.09	-1062.58	-1060.55
	5	-1064.40	-1115.90	-1099.80	-1045.23	-1068.75	-1066.24
	6	-1058.10	-1120.00	-1092.70	-1054.15	-1062.67	-1062.05
	7	-1088.00	-1124.00	-1116.90	-1049.07	-1052.49	-1052.29
X	8	-1096.70	-1137.20	-1129.90	-995.41	-1001.23	-1000.23
	9	-1146.50	-1174.40	-1162.00	-1044.02	-1027.52	-1027.40
	10	-1142.20	-1175.50	-1168.70	-984.32	-993.47	-991.45
	11	-1080.20	-1110.00	-1106.60	-1036.01	-1016.34	-1014.70
Ku	12	-1127.50	-1157.60	-1149.80	-1002.42	-998.24	-994.76
	13	-1092.10	-1136.30	-1115.80	-1030.28	-1010.20	-1008.99
	14	-1097.10	-1130.50	-1118.40	-1033.04	-1033.95	-1033.17
	15	-1081.50	-1123.70	-1098.80	-1007.27	-1006.10	-1005.37
	16	-1104.60	-1140.80	-1133.80	-1030.40	-1037.32	-1032.19
	17	-1099.90	-1108.90	-1106.30	-1055.82	-1041.13	-1038.39
K	18	-1129.00	-1145.40	-1141.10	-1039.10	-1038.39	-1035.48
	19	-1109.40	-1128.10	-1121.80	-1081.46	-1090.10	-1089.30
	20	-1135.30	-1152.30	-1145.30	-1076.61	-1073.86	-1073.85
	21	-1133.20	-1159.90	-1155.60	-1026.43	-1033.01	-1030.72
	22	-1087.40	-1113.90	-1107.60	-1062.99	-1060.54	-1059.42
	23	-1076.80	-1110.40	-1100.70	-1015.22	-1021.06	-1020.61
	24	-1062.10	-1089.50	-1077.00	-1004.97	-1007.37	-1003.88
	25	-1122.60	-1157.70	-1142.70	-1049.77	-1040.07	-1039.85
	26	-1146.60	-1163.40	-1159.90	-1038.44	-1028.96	-1028.95
Ka	27	-1156.90	-1166.90	-1164.80	-1107.92	-1089.18	-1089.17
	28	-1151.90	-1174.60	-1172.00	-1068.59	-1081.49	-1081.34
	29	-1104.10	-1123.20	-1112.60	-1139.89	-1145.89	-1145.78
	30	-1120.70	-1132.30	-1130.90	-1113.89	-1114.04	-1111.12
	31	-1080.60	-1114.20	-1081.80	-1030.50	-1012.28	-1011.99
	32	-1105.80	-1147.20	-1136.60	-1021.25	-1019.82	-1018.82
	33	-1098.10	-1135.80	-1133.10	-1069.92	-1061.36	-1060.54
	34	-1116.90	-1160.20	-1158.40	-1094.89	-1105.99	-1105.75
	35	-1134.30	-1166.80	-1155.60	-1074.50	-1070.67	-1069.99
	36	-1140.70	-1154.30	-1151.20	-1052.20	-1049.70	-1049.10
	37	-1125.90	-1135.50	-1132.30	-1078.90	-1063.80	-1062.50
	38	-1137.30	-1158.40	-1157.80	-1094.30	-1082.60	-1080.90
	39	-1141.40	-1159.20	-1156.90	-1058.10	-1055.80	-1054.60
	40	-1132.60	-1148.10	-1146.70	-1073.90	-1070.40	-1070.10

Location, with $R^{\text{ABS}} = 0.6$. The Normal distribution does not provide the highest LLK for either material.

For PEC, the Extreme Value distribution provides the highest LLK scores across all frequencies except $f_i = 2$ GHz. This consistent ranking indicates that, within the candidate set considered in this study, the shape of the PEC RCS distributions is more closely represented by the Extreme Value model. This behavior may be associated with the angular variability and asymmetry of the scattering response produced by the UAV geometry under the PEC assumption. However, the selection of the Extreme Value distribution should not be interpreted as resulting solely from the higher absolute RCS values observed for PEC.

For the ABS model, the distribution providing the highest LLK alternates between the Extreme Value and t-Location models, indicating a frequency-dependent change in the shape of the RCS distribution rather than a consistent preference for a single statistical model. At frequencies where the t-Location

distribution provides the highest LLK, the RCS samples are more closely represented by its approximately symmetric shape and heavier tails relative to the Normal distribution. At frequencies where the Extreme Value distribution provides the highest LLK, the angular RCS samples exhibit a distributional shape that is more closely represented by the Extreme Value model.

Overall, the different model-selection patterns obtained for PEC and ABS indicate that the electromagnetic material assumption affects not only the magnitude and variability of the simulated RCS, but also the statistical shape of its angular fluctuations. While the PEC model exhibits a nearly uniform preference for the Extreme Value distribution over the investigated frequency range, the frequency-dependent dielectric ABS model alternates between Extreme Value and t-Location. This result reinforces the importance of the material model when statistically characterizing UAV RCS and shows that conclusions obtained from an ideal PEC representation should not necessarily be generalized to dielectric target models.

The differences in LLK reported here should not be interpreted as proportional changes in radar detection performance. Different fitted RCS distributions may lead to different predicted values of P_d, since the RCS affects the target-return statistics under H_1. Conversely, P_{fa} is primarily determined by the noise/clutter statistics under H_0 and the detection threshold. Quantifying the resulting changes in P_d requires a complete radar detection model and is beyond the scope of this work.

It should be noted that the distribution-fitting results reported above are specific to the horizontal polarization considered in this work. Other co- or cross-polarized channels may modify the angular RCS statistics and, consequently, the estimated distribution parameters and LLK ranking. A systematic assessment of polarization effects on the RCS statistical modeling is left for future work.

V. Conclusion

This work performed statistical analysis and modeling of the RCS of the DJI Phantom IV Pro, investigating the influence of radar frequency and electromagnetic material assumptions on its angular RCS statistics. Using Feko® software, simulations were performed from 1 to 40 GHz and for azimuth angles from 0° to 359°, assuming the UAV body material as either PEC or ABS plastic. Extreme Value, Normal, and t-Location distributions were evaluated using log-likelihood scores to characterize the frequency-dependent statistical behavior of the resulting RCS datasets.

Numerical results show that the UAV body material as PEC consistently produces higher, more stable mean RCS values with a broader standard deviation, with the Extreme Value distribution providing the highest LLK among the candidate models at almost all frequencies. In contrast, the ABS plastic assumption exhibits lower RCS values and stronger frequency-dependent variations in the mean RCS, which may be associated with resonance and interference effects in the electromagnetic scattering response. For the ABS model, the distribution providing the highest LLK alternates between Extreme Value and t-Location depending on frequency. These results indicate that the electromagnetic material assumption affects not only the magnitude and angular variability of the simulated RCS, but also the statistical shape of its angular fluctuations.

The frequency-dependent RCS statistics also have practical implications for radar sensing. Changes in the RCS distribution modify the probability that the target RCS exceeds the minimum value required to produce a received signal above a specified receiver threshold, as demonstrated by the exceedance analysis. However, this probability should not be interpreted directly as the probability of detection, since P_d additionally depends on the receiver architecture, detection algorithm, noise and clutter statistics, integration strategy, and false-alarm requirements.

The additional numerical benchmark showed good agreement between RL-GO and the analytical PEC-sphere solution for electrically large targets, while also indicating increased discrepancy at smaller electrical sizes. Therefore, the UAV results at the lower-frequency end of the investigated range should be interpreted with greater caution. The statistical conclusions are also conditional on the horizontal polarization, fixed rotor configuration, external-body electromagnetic model, and candidate probability distributions considered in this study. Future work should investigate full-wave modeling at lower frequencies, internal UAV components, polarization, and rotor-orientation effects, as well as their impact on radar detection performance.

References

[1] D. White, M. Jahangir, C. J. Baker, and M. Antoniou, "Urban bird-drone classification with synthetic micro-doppler spectrograms," *IEEE Trans. Radar Syst.*, vol. 2, pp. 167–179, 2024, doi: 10.1109/TRS.2023.3326317.

[2] J.-P. Yaacoub *et al.*, "Security analysis of drones systems: Attacks, limitations, and recommendations," *Internet of Things*, vol. 11, p. 100218, 2020, doi: 10.1016/j.iot.2020.100218.

[3] O. A. Krasnov, X. Li, and A. Yarovoy, "Model-based signal processing for joint drones detection, tracking, and parameters estimation," *IEEE Trans. Radar Syst.*, vol. 2, pp. 880–898, 2024, doi: 10.1109/TRS.2024.3458150.

[4] A. Coluccia, G. Parisi, and A. Fascista, "Detection and classification of multirotor drones in radar sensor networks: A review," *Sensors*, vol. 20, no. 15, 2020, doi: 10.3390/s20154172. [Online]. Available: https://www.mdpi.com/1424-8220/20/15/4172

[5] M. M. Rios, M. da Silva Borges, J. R. d. S. Filho, and V. Fernandes, "Radar monitoring of estuarine fronts in Guanabara Bay, Southeastern Brazil," in *2025 Workshop on Communication Networks and Power Systems (WCNPS)*, Nov 2025, pp. 1–6, doi: 10.1109/WCNPS69127.2025.11295863.

[6] M. Da Silva Borges, R. B. Di Renna, and V. Fernandes, "Distributed UAV detection and classification in cell-free ISAC with real RCS signatures," in *2026 IEEE International Mediterranean Conference on Communications and Networking (MeditCom)*, July 2026, pp. 1–6, doi: 10.1109/MeditCom67211.2026.11641072.

[7] N. Kumar, A. Dasgupta, V. Satyanand Mutnuri, and R. Pachamuthu, "An efficient approach for calibration of automotive radar–camera with real-time projection of multimodal data," *IEEE Trans. Radar Syst.*, vol. 2, pp. 573–582, 2024, doi: 10.1109/TRS.2024.3408231.

[8] I. K. Kapoulas, A. Hatziefremidis, A. K. Baldoukas, E. S. Valamontes, and J. C. Statharas, "Small fixed-wing UAV radar cross-section signature investigation and detection and classification of distance estimation using realistic parameters of a commercial anti-drone system," *Drones*, vol. 7, no. 1, 2023, doi: 10.3390/drones7010039. [Online]. Available: https://www.mdpi.com/2504-446X/7/1/39

[9] V. Semkin, J. Haarla, T. Pairon, C. Slezak, S. Rangan, V. Viikari, and C. Oestges, "Analyzing radar cross section signatures of diverse drone models at mmWave frequencies," *IEEE Access*, vol. 8, pp. 48 958–48 969, 2020, doi: 10.1109/ACCESS.2020.2979339.
[10] T. O. Costalonga, V. P. R. Magri, and V. Fernandes, "Detecção de drone quadrotor por radar pulsado de banda X," in *XLI Simp. Brasileiro de Telecom. e Processamento de Sinais*, 2023, doi: 10.14209/sbrt.2023.1570923747.
[11] R. Fu, M. A. Al-Absi, K.-H. Kim, Y.-S. Lee, A. A. Al-Absi, and H.-J. Lee, "Deep learning-based drone classification using radar cross section signatures at mmWave frequencies," *IEEE Access*, vol. 9, pp. 161 431–161 444, 2021, doi: 10.1109/ACCESS.2021.3115805.
[12] P. Sedivy and O. Nemec, "Drone RCS statistical behaviour," in *Proceedings of the MSG-SET-183 Specialists' meeting on "Drone Detectability: Modelling the Relevant Signature". North Atlantic Treaty Organization (NATO), Held Virtually (via WebEx)*, 2021, pp. 1–4.
[13] T. O. Costalonga, W. S. L. Soares, V. P. R. Magri, and V. Fernandes, "Statistical analysis and modeling of a quadrotor's radar cross-section," in *2023 Workshop on Communication Networks and Power Systems (WCNPS)*, 2023, pp. 1–7, doi: 10.1109/WCNPS60622.2023.10345285.
[14] K. P. Burnham and D. R. Anderson, *Model Selection and Multimodel Inference: A Practical Information-Theoretic Approach*, 2nd ed. New York, NY: Springer, 2002, doi: 10.1007/b97636.
[15] V. Fernandes, T. F. A. Nogueira, H. V. Poor, and M. V. Ribeiro, "Statistical modeling of energy harvesting in hybrid PLC-WLC channels," *Sustainability*, vol. 14, no. 1, 2022, doi: 10.3390/su14010442. [Online]. Available: https://www.mdpi.com/2071-1050/14/1/442
[16] DJI, "Phantom 4 Pro V2.0," [Online]. Available: https://www.dji.com/br/phantom-4-pro-v2, accessed: Oct. 28, 2024.
[17] M. Pérez-Escribano and E. Márquez-Segura, "Parameters characterization of dielectric materials samples in microwave and millimeter-wave bands," *IEEE Trans. Microw. Theory Techn.*, vol. 69, no. 3, pp. 1723–1732, 2021, doi: 10.1109/TMTT.2020.3045211.
[18] T. Pető, S. Bilicz, L. Szűcs, S. Gyimóthy, and J. Pávó, "The radar cross section of small propellers on unmanned aerial vehicles," in *2016 10th European Conference on Antennas and Propagation (EuCAP)*, 2016, pp. 1–4, doi: 10.1109/EuCAP.2016.7481645.
[19] E. Lansey, G. Hankins, I. Mandel, R. Martelly, J. Slater, and N. R. Greenberg, "In defense of spheres for computational electromagnetics code validation and benchmarking: Rethinking the sphere of influence," *IEEE Antennas Propag. Mag.*, vol. 67, no. 2, pp. 87–94, 2025, doi: 10.1109/MAP.2025.3537414.
[20] C. Balanis, *Balanis' Advanced Engineering Electromagnetics*. Wiley, 2023. [Online]. Available: https://books.google.com.br/books?id=w-LqEAAAQBAJ
[21] T. O. Costalonga, "Unmanned aircraft system's radar detection: Statistical analysis and modeling of the radar-cross section," Master's thesis, Universidade Federal Fluminense, Niterói, RJ, Brazil, 2024.
[22] J. Beirlant, Y. Goegebeur, J. Segers, and J. L. Teugels, *Statistics of extremes: theory and applications*. John Wiley & Sons, 2006.
[23] "IEEE Standard Letter Designations for Radar-Frequency Bands," IEEE Std 521-2019 (Revision of IEEE Std 521-2002), pp. 1–15, 2020, doi: 10.1109/IEEESTD.2020.8999849.



Tiago Ogioni Costalonga received the B.Sc. degree in Electrical Engineering from the Federal University of Viçosa (UFV), Brazil, in 2013, the postgraduate degree in Weapon Control Systems from the Pontifical Catholic University of Rio de Janeiro (PUC-RJ) in 2020, and the M.Sc. degree in Electrical and Telecommunications Engineering from Fluminense Federal University (UFF), Brazil, in 2024. He currently serves as the Coordinator of Electronic Warfare Post-graduation for Officers at the Admiral Alexandrino Instruction Center (CIAA) in Rio de Janeiro, RJ, Brazil. His research interests include control systems, embedded systems, automation, telecommunications, antennas, radars, and their applications in both military and civilian sectors.



Vanessa Przybylski Ribeiro Magri is an Electrical Engineer with emphasis on Telecommunications, she completed her D.Sc. degree at PUC-Rio in 2011. She completed her Post-Doctorate in a Project linked to the National Institute for Space Research (INPE), the National Institute of Science and Technology, CETUC-PUC-Rio, and the National Institute of Space Technologies. Her career began as a professor in the Department of Telecommunications Engineering (TET) at Fluminense Federal University (UFF) in 2013. Currently, she works as the coordinator of LAPROP (UFF Antennas and Propagation Laboratory).



Victor Fernandes received his D.Sc. degree in Electrical Engineering from the Federal University of Juiz de Fora (UFJF), Brazil, in 2021. Since 2021, he has been an assistant professor in the Department of Telecommunications Engineering at the Fluminense Federal University (UFF) and a permanent professor in the Postgraduate Program in Electrical and Telecommunications Engineering (PPGEET) in Brazil. From 2025 to 2026, he was a Visiting Professor at ISAE-SUPAERO, Toulouse, France. His research interests include signal processing, communications theory applied to wireless and power line systems, and radar detection.